A quality-hierarchical temperature imaging network for TDLAS tomography

Si, Jingjing; Fu, Gengchen; Cheng, Yinbo; Zhang, Rui; Enemali, Godwin; Liu, Chang

Published in:
IEEE Transactions on Instrumentation and Measurement

DOI:
10.1109/TIM.2022.3144211

Publication date:
2022

Document Version
Author accepted manuscript

A Quality-Hierarchical Temperature Imaging Network for TDLAS Tomography

Jingjing Si, *Member*, *IEEE*, Gengchen Fu, Yinbo Cheng, Rui Zhang, Godwin Enemali, *Member*, *IEEE*, Chang Liu, *Member*, *IEEE*

***Abstract*—Tunable diode laser absorption spectroscopy (TDLAS) tomography is a well-established combustion diagnostic technique for imaging two-dimensional cross-sectional distributions of critical flow-field parameters. As two key metrics in TDLAS tomography, reconstruction accuracy and efficiency are generally traded off to satisfy either the requirement of high-fidelity image retrieval or rapid tomographic data inversion. In this paper, a novel quality-hierarchical temperature imaging network for TDLAS tomography is developed based on stacked Long Short Term Memory (LSTM). From limited line-of-sight TDLAS measurements, this network outputs two reconstructed temperature images, i.e. a coarse-quality image and a fine-quality image, with different numbers of network layers and consequently different computational costs. The coarse-quality image provides more timely temperature reconstruction, which can satisfy real-time dynamic monitoring of turbulence–chemistry interactions with a temporal resolution of tens of kilo frames per second. On the other hand, the fine-quality image, that can be stored and utilized for offline analysis and diagnosis, further details the temperature reconstruction with more accurate features. Both numerical stimulation and lab-scale experiment validated the accuracy-efficiency trade-off achieved by the proposed quality-hierarchical temperature imaging network.**

***Index Terms*—Long Short Term Memory (LSTM), tomography, Tunable Diode Laser Absorption Spectroscopy (TDLAS), temperature imaging, temporal resolution.**

I. Introduction

With the rapid progress in imaging theories and sensing technologies, laser tomography has been a versatile imaging technique and has attracted extensive research efforts. Tunable Diode Laser Absorption Spectroscopy (TDLAS) tomography is a powerful tool for *in situ* combustion diagnostic, attributing to its non-invasive imaging of two-dimensional (2-D) cross-sectional distributions of critical flow-field parameters, such as temperature [1], species concentration [2,3], and velocity [4], in reactive flows with high sensitivity.

Computational tomographic algorithms, such as Algebraic Reconstruction Technique (ART) [5], Simultaneous Algebraic Reconstruction Technique (SART) [6], Landweber algorithm [7], and the most recent entropy regularization [8], have been well developed for TDLAS tomographic reconstruction. Among them, the two-line strategy [9] is widely adopted for temperature imaging, in which the pixel-wise temperature is retrieved from the reconstructed absorbance coefficients at two spectral transitions with different temperature-dependent line strengths. Since the number of available line-of-sight (LoS) TDLAS measurements is limited in many practical applications when the optical access is restricted [10], the inverse problem involving reconstructing absorbance coefficients is inherently ill-posed, resulting into severe artefacts in the tomographic images. Alternatively, multispectral tomographic algorithms [11, 12] can reconstruct temperature distributions by enhancing the sampling in the spectral domain through broadband absorption spectroscopy. However, this kind of methods suffers from extremely high computational cost which can take a few hours only for a single-frame reconstruction.

With the rapid development of artificial intelligence, deep learning algorithms [13-15] have been recently applied to TDLAS tomography and other optical imaging techniques [16-20]. If *a priori* information, such as field distribution, thermochemistry properties of the target flow, is predictable or well known, deep learning algorithms can effectively train the implicit relationship between the forward model and projection measurements, resulting into more rapid and more accurate image reconstruction. Pioneering tomographic algorithms based on Extreme Learning Machine (ELM) [21] and Convolutional Neural Network (CNN) [22, 23] were developed for TDLAS tomography with densely spatial sampling, i.e. beam arrangements with at least 6 angular projection views and tens of laser beams per view. To address the practical deployment of TDLAS tomographic sensor with limited optical access, we proposed two CNN-aided algorithms to reconstruct the distributions of flame temperature and species concentration with only 32 laser beams, i.e. 4 angular projection views and 8 laser beams per view [24, 25].

Among all the above data-driven efforts, once optimally trained, the network reconstructs the distributions of flow-field parameters with fixed accuracy and temporal resolution. In practice, these two key metrics in TDLAS tomography, i.e.

This work was supported in part by the National Natural Science Foundation of China under Grant 61701429, the U.K. Engineering and Physical Sciences Research Council under Platform Grant EP/P001661/1, and the Natural Science Foundation of Hebei Province under Grant F2021203027. *(Corresponding author: Chang Liu.)*

J. Si and G. Fu are with the School of Information Science and Engineering, Yanshan University, Qinhuangdao 066004, China. J. Si is also with the Hebei Key Laboratory of Information Transmission and Signal Processing, Qinhuangdao 066004, China.

Y. Cheng is with the Ocean College, Hebei Agricultural University, Qinhuangdao 066003, China.

R. Zhang, G. Enemali, and C. Liu are with the School of Engineering, University of Edinburgh, Edinburgh EH9 3JL, U.K. (e-mail: C.Liu@ed.ac.uk).

reconstruction accuracy and efficiency, are traded off to satisfy either the requirement of high-fidelity image retrieval or rapid tomographic data inversion. A more sophisticated architecture of the network can generally learn more complex data inversion processes and contribute to better reconstruction accuracy, however, at the cost of longer inference time. The inference time, i.e. temporal response of TDLAS tomography, is critically important for online combustion monitoring, in which instantaneous imaging is highly demanded to indicate the combustion condition and provide real-time feedback for active control. On the contrary, a simpler architecture benefits faster image reconstruction but may be invalid for combustion optimization where detailed features should be reconstructed with penetrating accuracy. Therefore, a purpose driven image reconstruction strategy is imperative for trading off between accuracy and efficiency in TDLAS tomography.

To address this issue, a novel quality-hierarchical temperature imaging neural network is proposed for TDLAS tomography based on stacked Long Short Term Memory (LSTM) [26, 27]. LSTM is exploited to capture the inherent correlations among LoS measurements attributing to their spatial layout in a TDLAS tomographic sensor. The stacked architecture is established to realize progressive reconstruction with its depth-improved representational capacity. From limited LoS TDLAS measurements, this network outputs two temperature images of the entire sensing region: (a) a coarse snapshot of combustion field for online evaluation of instantaneous combustion condition, and (b) a fine description of the 2-D cross-sectional temperature distribution for detailed offline analysis of the combustion process. To the best of our knowledge, it is the first time to discuss a progressive tomographic algorithm for TDLAS tomographic system based on deep learning. Scientifically and technically extended from the conference version [28], both simulation and lab-scale experiment are carried out in this paper to validate the proposed quality-hierarchical temperature imaging algorithm.

The remainder of this paper is organized as follows. The mathematical background of TDLAS tomography is introduced in Section II. Then, the quality-hierarchical temperature imaging network is established using the 32-beam TDLAS tomographic sensor in Section III. Subsequently, the established network is trained and its performance is examined by simulated data and lab-scale experimental data in Sections IV and V, respectively. Finally, a brief conclusion is presented in Section VI.

II. Mathematical Background

When a laser beam at frequency v [cm^{-1}] penetrates an absorbing gas sample through a path of length L [cm], a proportion of its intensity is absorbed. The path integrated absorbance A_v [cm^{-1}] is formulated as

$$A_v = \int_0^L a_v(l)dl = \int_0^L P(l)\cdot C(l)\cdot S_v(T(l))\ dl\ , \qquad (1)$$

where l denotes the local position along the path, $P(l)$ [atm], $C(l)$ and $T(l)$ [K] are the local pressure, concentration and temperature of the absorbing species at l, respectively. $S_v(\cdot)$ [cm^{-2}atm^{-1}] denotes the temperature-dependent line strength.

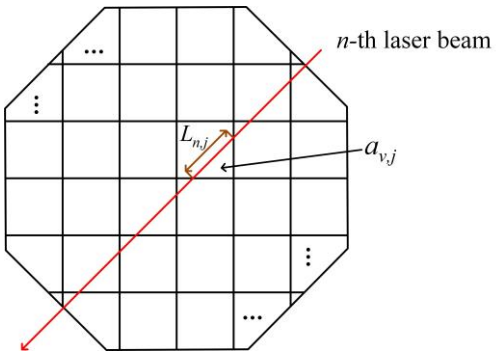

Fig. 1. Geometric description of a LoS TDLAS measurement in an octagonal sensing region.

$a_v(l)$ [cm^{-2}] is the local density of A_v, satisfying $a_v(l)=P(l)\cdot C(l)\cdot S_v(T(l))$.

As shown in Fig. 1, if the sensing region is discretized into J pixels and the flow-field parameters are assumed to be uniform in each pixel, the path integrated absorbance $A_{v,n}$ of the n-th laser beam can be written as

$$A_{v,n} = \sum_{j=1}^{J}(a_{v,j}\cdot L_{n,j})\cdot \qquad (2)$$

The absorbance density $a_{v,j}$ in the j-th pixel is

$$a_{v,j} = P\cdot C_j\cdot S_v(T_j)\,, \qquad (3)$$

where $L_{n,j}$ is the chord length of the n-th laser beam within the j-th pixel. C_j and T_j are species concentration and temperature in the j-th pixel, respectively. P is the local pressure. Given unconfined flames, P is assumed to be 1 atm in the sensing region. In Fig. 1, the sensing region is defined as octagonal to be consistent with the optical layout introduced later in Section III.

For simplicity, a path integrated absorbance vector $\boldsymbol{A}_v\in\mathbb{R}^{N\times 1}$, which is formed by $[A_{v,1}, A_{v,2},\ldots, A_{v,N}]$ measured by the N laser beams, can be denoted as

$$\boldsymbol{A}_v = \boldsymbol{L}\boldsymbol{a}_v = P\boldsymbol{L}\ \boldsymbol{C}\otimes S_v(\boldsymbol{T})\ , \qquad (4)$$

where $\boldsymbol{L}\in\mathbb{R}^{N\times J}$ is the chord length matrix with elements $L_{n,j}$, $n\in\{1,2,...,N\}$, $j\in\{1,2,...,J\}$. Absorbance density vector $\boldsymbol{a}_v\in\mathbb{R}^{J\times 1}$, temperature vector $\boldsymbol{T}\in\mathbb{R}^{J\times 1}$, and species concentration vector $\boldsymbol{C}\in\mathbb{R}^{J\times 1}$ are formed as $\boldsymbol{a}_v = [a_{v,1}, a_{v,2}, \ldots, a_{v,J}]^{\mathrm{T}}$, $\boldsymbol{T}=[T_1, T_2, \ldots, T_J]^{\mathrm{T}}$, and $\boldsymbol{C} = [C_1, C_2, \ldots, C_J]^{\mathrm{T}}$, respectively. $\otimes$ represents element-wise multiplication.

Given (4), the inverse problem of temperature imaging in TDLAS tomography can be described as retrieval of temperature vector $\boldsymbol{T}$, that is coupled in $\boldsymbol{a}_{v_1},\ldots,\boldsymbol{a}_{v_W}$, from path integrated absorbance vectors $\boldsymbol{A}_{v_1},\ldots,\boldsymbol{A}_{v_W}$ measured at W absorption transitions. For the two-line method, two transitions with different temperature sensitivity are used, i.e. W=2. Since the total number of LoS TDLAS measurements, $2N$, in $\boldsymbol{A}_{v_1}$ and $\boldsymbol{A}_{v_2}$ is significantly less than the number of pixel-wise temperature values J in $\boldsymbol{T}$ to be reconstructed, this inverse problem is seriously ill-posed. In this work, a quality-hierarchical temperature imaging neural network is developed to solve this inverse problem progressively.

III. Network Establishment

A. System Specification

To facilitate the presentation of the proposed quality-hierarchical temperature imaging network, the optical layout of our lab-scale 32-beam TDLAS tomographic sensor is introduced in this subsection. As shown in Fig. 2, the 32 laser beams are arranged in 4 equiangular projection angles, each angle with 8 equispaced parallel beams. The distance between the adjacent parallel beams is 18 mm, which makes the octagonal sensing region with side length of 144 mm. More details of the optics and electronics were described in our previous publications [8, 29]. The proposed QHT-LSTM can also be generally applied with a different beam arrangement, in which the TDLAS tomographic inverse problem satisfies equation (4).

As a major product of combustion, water vapor (H_2O) is chosen as the target absorbing species for imaging the flow-field parameters. Two H_2O absorption transitions at v_1=7185.6 cm^{-1} and v_2=7444.36 cm^{-1} are adopted due to their moderate line strengths and good temperature sensitivity over the target temperature range of 300-1200 K [30]. Path integrated absorbances $\boldsymbol{A}_{v_1}\in\mathbb{R}^{32\times1}$ and $\boldsymbol{A}_{v_2}\in\mathbb{R}^{32\times1}$ are measured by the 32-beam sensor at v_1 and v_2, respectively.

To guarantee the physical integrity of the forward problem, the temperature distribution in the entire sensing region is reconstructed. The sensing region is discretized into 7592 uniform pixels, each with dimensions of 3.6 mm×3.6 mm. Irregular pixels truncated by the boundary of the octagon are ignored. The quality-hierarchical temperature imaging network is constructed in this work to progressively reconstruct the temperature vector $\boldsymbol{T}\in\mathbb{R}^{7592\times1}$ from $\boldsymbol{A}_{v_1}$ and $\boldsymbol{A}_{v_2}$.

B. Data rearrangement

To facilitate the inverse mapping from LoS TDLAS measurements to the temperature distribution with LSTM, a data rearrangement strategy is introduced for TDLAS measurements, which is shown in Algorithm 1. Path integrated absorbances $\boldsymbol{A}_{v_1}\in\mathbb{R}^{N\times1}$ and $\boldsymbol{A}_{v_2}\in\mathbb{R}^{N\times1}$, measured by N laser beams placed in R equiangular projection angles, are rearranged into a sequence of vectors $\overline{\boldsymbol{A}}_1, \overline{\boldsymbol{A}}_2,..., \overline{\boldsymbol{A}}_Q$, where $\overline{\boldsymbol{A}}_q\in\mathbb{R}^{2R\times1}$, $q\in\{1, 2,..., Q\}$, Q is the total number of equispaced parallel beams in each projection angle. N=R×Q.

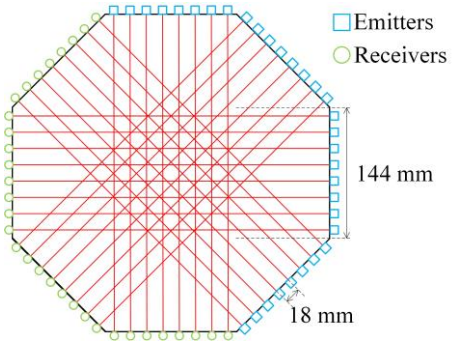

Fig. 2. Beam arrangement for the TDLAS tomographic sensor in the sensing region.

Algorithm 1 Data rearrangement for TDLAS measurements

Input: Number of equiangular projections R, number of equispaced parallel beams Q, path integrated absorbances $\boldsymbol{A}_{v_1}\in\mathbb{R}^{N\times1}$ and $\boldsymbol{A}_{v_2}\in\mathbb{R}^{N\times1}$, where N=R×Q.

Initialize:

For q=1 to Q **do**

$\overline{\boldsymbol{A}}_q$←zeros(2$R$, 1)

End for

Operations:

1: $\boldsymbol{A}_{v_1}^{\text{reshape}}$ ← reshape($\boldsymbol{A}_{v_1}$, (R, Q))

$\boldsymbol{A}_{v_2}^{\text{reshape}}$ ← reshape($\boldsymbol{A}_{v_2}$, (R, Q))

For q=1 to Q **do**

2: $\overline{\boldsymbol{A}}_q$←Concat($\boldsymbol{A}_{v_1}^{\text{reshape}}$(:, q), $\boldsymbol{A}_{v_2}^{\text{reshape}}$(:, q))

End for

3: $\overline{\boldsymbol{A}}$←{$\overline{\boldsymbol{A}}_q\in\mathbb{R}^{2R\times1}$: q=1,...,Q}

Output: $\overline{\boldsymbol{A}}$

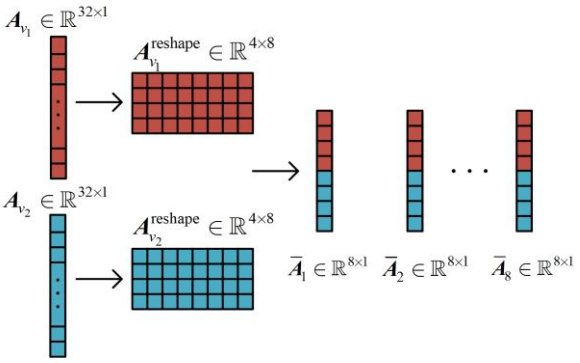

Fig. 3. Data rearrangement of the path integrated absorbances measured by the 32-beam TDLAS tomographic sensor at two transitions.

Firstly, $\boldsymbol{A}_{v_1}\in\mathbb{R}^{N\times1}$ and $\boldsymbol{A}_{v_2}\in\mathbb{R}^{N\times1}$ are reshaped into matrices $\boldsymbol{A}_{v_1}^{\text{reshape}}\in\mathbb{R}^{R\times Q}$ and $\boldsymbol{A}_{v_2}^{\text{reshape}}\in\mathbb{R}^{R\times Q}$, respectively. Element in the q-th column and the p-th row is the path integrated absorbance obtained from the q-th parallel laser beam at the p-th projection angle. $p\in\{1, 2,..., R\}$, $q\in\{1, 2,..., Q\}$. Then, the q-th columns $\boldsymbol{A}_{v_1}^{\text{reshape}}(:, q)\in\mathbb{R}^{R\times1}$ and $\boldsymbol{A}_{v_2}^{\text{reshape}}(:, q)\in\mathbb{R}^{R\times1}$ of matrices $\boldsymbol{A}_{v_1}^{\text{reshape}}$ and $\boldsymbol{A}_{v_2}^{\text{reshape}}$ are concatenated into vector $\overline{\boldsymbol{A}}_q\in\mathbb{R}^{2R\times1}$ for q=1, 2,…., Q. Consequently, all elements in $\overline{\boldsymbol{A}}_q$ are path integrated absorbances obtained from the q-th parallel laser beam. Finally, $\overline{\boldsymbol{A}}_1, \overline{\boldsymbol{A}}_2,..., \overline{\boldsymbol{A}}_Q$ form the sequence of vectors $\overline{\boldsymbol{A}}$=$\{\overline{\boldsymbol{A}}_1, \overline{\boldsymbol{A}}_2,..., \overline{\boldsymbol{A}}_Q\}$. Neighboring vectors in $\overline{\boldsymbol{A}}$ present inherent similarities since their elements are obtained from adjacent parallel beams.

Taking the optical layout of our 32-beam TDLAS tomographic sensor as an example, Fig. 3 demonstrates the rearrangement of the path integrated absorbances $\boldsymbol{A}_{v_1}\in\mathbb{R}^{32\times1}$ and $\boldsymbol{A}_{v_2}\in\mathbb{R}^{32\times1}$ into sequential vectors $\overline{\boldsymbol{A}}_1, \overline{\boldsymbol{A}}_2,..., \overline{\boldsymbol{A}}_8$, which will be taken as the input of the quality-hierarchical temperature imaging network constructed in the following subsection.

C. Network implementation

A Quality-Hierarchical Temperature imaging network based on stacked LSTM (QHT-LSTM) is established for the two-step reconstruction of temperature distribution in the sensing region.

LSTM is a variant of Recurrent Neural Networks (RNN) designed to be better at storing and accessing information than the standard RNN. Benefiting from purpose-build memory cells, LSTM is better at finding and exploiting global features than CNN. Due to the smoothness of the distributions of combustion parameters in reactive flows, LoS TDLAS measurements obtained by TDLAS tomographic sensor generally preserve both local and global correlations. Here, stacked LSTM is established to realize quality-hierarchical image reconstruction while taking full utilities of the statistical correlations across sequential vectors rearranged from LoS TDLAS measurements.

The overall architecture of QHT-LSTM is shown in Fig. 4. This network is composed of three LSTM layers, i.e. LSTM1, LSTM2, and LSTM3, and four fully-connected (FC) layers, i.e. FC1, FC2, FC3, and FC4. Taking sequential vectors $\overline{\boldsymbol{A}}_1, \overline{\boldsymbol{A}}_2,..., \overline{\boldsymbol{A}}_Q$ as input, the first step is to rapidly output a coarse-quality temperature vector $\widehat{\boldsymbol{T}}_{\text{coarse}}$ for real-time monitoring, while the second step is to obtain a fine-quality temperature vector $\widehat{\boldsymbol{T}}_{\text{fine}}$ for more accurate offline analysis.

Each LSTM layer consists of Q units. The internal structure of the t-th unit is shown in Fig. 5, $t \in \{1, 2,..., Q\}$. It contains input gate $\boldsymbol{i}_t$, forget gate $\boldsymbol{f}_t$, output gate $\boldsymbol{o}_t$ and memory cell $\boldsymbol{C}_t$. The forget gate can reset the cell variable which leads to "forgetting" the stored input $\boldsymbol{C}_{t-1}$. The input and output gates are used for reading input from $\boldsymbol{x}_t$ and writing output to $\boldsymbol{h}_t$, respectively. The memory cell is used to store the state information in the network. The calculation formulas of the forget gate, input gate, memory cell and output gate are described in (5)-(8), respectively.

$$\boldsymbol{f}_t = \sigma(\boldsymbol{W}_f[\boldsymbol{h}_{t-1}, \boldsymbol{x}_t] + \boldsymbol{b}_f) \tag{5}$$

$$\boldsymbol{i}_t = \sigma(\boldsymbol{W}_i[\boldsymbol{h}_{t-1}, \boldsymbol{x}_t] + \boldsymbol{b}_i) \tag{6}$$

$$\boldsymbol{C}_t = \boldsymbol{f}_t \otimes \boldsymbol{C}_{t-1} + \boldsymbol{i}_t \otimes \tanh(\boldsymbol{W}_c[\boldsymbol{h}_{t-1}, \boldsymbol{x}_t] + \boldsymbol{b}_c) \tag{7}$$

$$\boldsymbol{h}_t = \sigma(\boldsymbol{W}_o[\boldsymbol{h}_{t-1}, \boldsymbol{x}_t] + \boldsymbol{b}_o) \otimes \tanh(\boldsymbol{C}_t) \tag{8}$$

where $\sigma(\cdot)$ and $\tanh(\cdot)$ represent the sigmoid and hyperbolic tangent activation function, respectively. $[\boldsymbol{h}_{t-1}, \boldsymbol{x}_t]$ is formed by concatenating $\boldsymbol{h}_{t-1}$ and $\boldsymbol{x}_t$. $\boldsymbol{W}_f \in \mathbb{R}^{H_f \times K_f}$ ($\boldsymbol{b}_f \in \mathbb{R}^{H_f \times 1}$), $\boldsymbol{W}_i \in \mathbb{R}^{H_i \times K_i}$ ($\boldsymbol{b}_i \in \mathbb{R}^{H_i \times 1}$), $\boldsymbol{W}_c \in \mathbb{R}^{H_c \times K_c}$ ($\boldsymbol{b}_c \in \mathbb{R}^{H_c \times 1}$) and $\boldsymbol{W}_o \in \mathbb{R}^{H_o \times K_o}$ ($\boldsymbol{b}_o \in \mathbb{R}^{H_o \times 1}$) are weight matrices (bias vectors) that would be trained for the forget gate, input gate, memory cell and output gate, respectively. H_f (K_f), H_i (K_i), H_c (K_c) and H_o (K_o) are the heights (widths) of the weight matrices. In this work, the hidden size in LSTM unit is set as 50, which determines H_f, H_i, H_c, and H_o. K_f, K_i, K_c, and K_o are determined by the lengths of inputs.

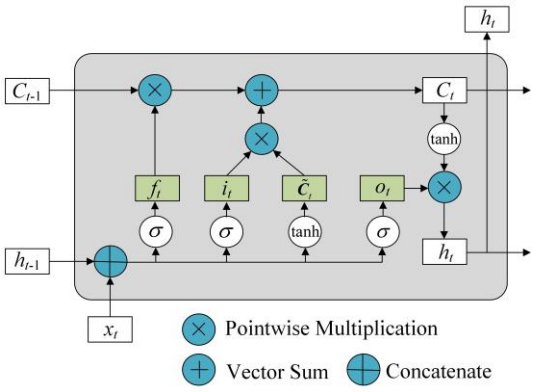

Fig. 5. The internal structure of the t-th unit in each LSTM layer.

In Fig. 4, (FCk, n_k) represents the k-th FC layer FCk with n_k neurons for $k \in \{1, 2, 3, 4\}$. Its forward propagation $\text{FC}_k(\cdot)$ can be formulated as

$$\boldsymbol{O}_k = \text{FC}_k(\boldsymbol{I}_k) = g(\boldsymbol{W}_k \boldsymbol{I}_k + \boldsymbol{b}_k), \tag{9}$$

where $\boldsymbol{I}_k$, $\boldsymbol{O}_k$, $\boldsymbol{W}_k$, $\boldsymbol{b}_k$ and $g(\cdot)$ are the input vector, output vector, weight matrix, bias vector and activation function, respectively. For a FC layer with C_I inputs and n_k neurons, the sizes of the weight matrix and the bias vector are $n_k \times C_I$ and $n_k \times 1$, respectively.

Taking the sequence of vectors $\overline{\boldsymbol{A}} = \{\overline{\boldsymbol{A}}_1, \overline{\boldsymbol{A}}_2,..., \overline{\boldsymbol{A}}_Q\}$ as the input, the feed-forward process of the proposed QHT-LSTM can be mathematically described as follows:

$$\boldsymbol{y}_{\text{LSTM1}} = \text{LSTM}_1(\overline{\boldsymbol{A}}) \tag{10}$$

$$\widehat{\boldsymbol{T}}_{\text{coarse}} = \text{FC}_1(\boldsymbol{y}_{\text{LSTM1}}) \tag{11}$$

$$\boldsymbol{y}_{\text{LSTM3}} = \text{LSTM}_3(\text{LSTM}_2(\text{LSTM}_1(\overline{\boldsymbol{A}}))) \tag{12}$$

$$\widehat{\boldsymbol{T}}_{\text{fine}} = \text{FC}_4(\text{FC}_3(\text{FC}_2(\boldsymbol{y}_{\text{LSTM3}}))) \tag{13}$$

where $\text{LSTM}_l(\cdot)$ denotes the forward propagation of the l-th LSTM layer LSTMl for $l \in \{1, 2, 3\}$. $\boldsymbol{y}_{\text{LSTM1}}$ and $\boldsymbol{y}_{\text{LSTM3}}$ are the outputs of LSTM1 and LSTM3 layers, which are used for reconstructing $\widehat{\boldsymbol{T}}_{\text{coarse}}$ and $\widehat{\boldsymbol{T}}_{\text{fine}}$, respectively.

By substituting (10) into (11) and substituting (12) into (13), the forward propagation process of the coarse layer $F_{\text{coarse}}(\cdot)$ and fine layer $F_{\text{fine}}(\cdot)$ of QHT-LSTM can be expressed as:

$$\widehat{\boldsymbol{T}}_{\text{coarse}} = F_{\text{coarse}}(\overline{\boldsymbol{A}}) = \text{FC}_1(\text{LSTM}_1(\overline{\boldsymbol{A}})) \tag{14}$$

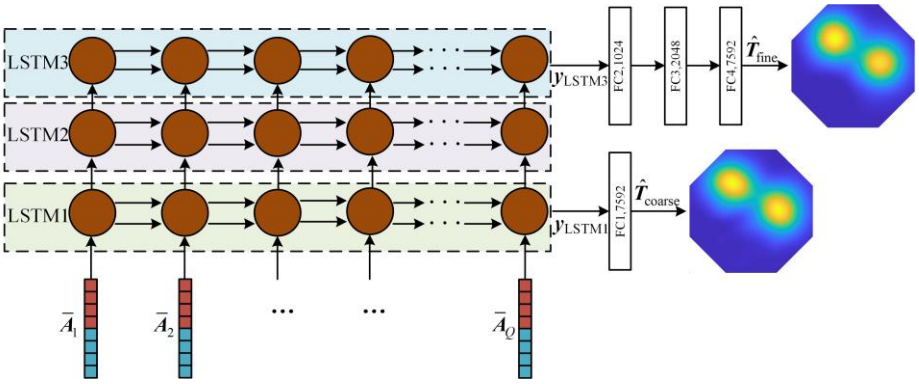

Fig. 4. The overall architecture of the proposed QHT-LSTM.

$$\hat{\boldsymbol{T}}_{\text{fine}} = F_{\text{fine}}(\bar{\boldsymbol{A}}) = \text{FC}_4(\text{FC}_3(\text{FC}_2(\text{LSTM}_3(\text{LSTM}_2(\text{LSTM}_1(\bar{\boldsymbol{A}})))))) \quad (15)$$

Compared with $F_{\text{coarse}}(\cdot)$, $F_{\text{fine}}(\cdot)$ involves higher computational cost, and consequently outputs reconstruction with better accuracy.

With quality-hierarchical outputs $\hat{\boldsymbol{T}}_{\text{coarse}}$ and $\hat{\boldsymbol{T}}_{\text{fine}}$, image reshaped from $\hat{\boldsymbol{T}}_{\text{coarse}}$ provides a faster but coarse temperature profile for the sensing region, while image reshaped from $\hat{\boldsymbol{T}}_{\text{fine}}$ gives a finer description of the 2-D cross-sectional temperature distribution but at the cost of longer computational time.

It is worth mentioning that stacked CNN can also realize similar quality-hierarchical temperature imaging by replacing LSTM layers in Fig. 4 with convolutional layers. However, we proved it with large simulation exercises that LSTM is superior over CNN to be the major structure in our network in terms of both reconstruction accuracy and efficiency.

IV. Network Training and Testing

A. Dataset

Phantoms with the different combinations of 2-D Gaussian inhomogeneities are constructed to simulate the multimodal hotspots in practical combustion processes. Since H_2O concentration is generally well-correlated with temperature in hydrocarbon flames [31], the distributions of temperature and H_2O concentration, i.e. $T(x, y)$ and $C(x, y)$, are similarly modeled as

$$T(x,y) = \sum_{m=1}^{M} \lambda_m \beta_m \exp\left[-\frac{(x-\mu_{x,m})^2+(y-\mu_{y,m})^2}{2\sigma_m^2}\right] + T_{\min} \quad (16)$$

$$C(x,y) = \sum_{m=1}^{M} \lambda_m \eta_m \exp\left[-\frac{(x-\mu_{x,m})^2+(y-\mu_{y,m})^2}{2\sigma_m^2}\right] + C_{\min} \quad (17)$$

where (x, y) denotes the coordinates of the sensing region. $x \in \{1, 2,...,96\}$ and $y \in \{1,2,...,96\}$. m and M denote the m-th and the total number of Gaussian inhomogeneities in the phantom, respectively. $(\mu_{x,m}, \mu_{y,m})$ represents the central location of the m-th Gaussian inhomogeneity. σ_m is the standard deviation along both x and y axes. $T_{\min}$ and $C_{\min}$ are the minimum temperature and H_2O concentration in the sensing region, respectively. λ_m, β_m and η_m are random scaling factors for the m-th Gaussian inhomogeneity. $\beta_m \sim U(T_{\text{peakL}}\text{-}T_{\min}, T_{\text{peakU}}\text{-}T_{\min})$, $\eta_m \sim U(C_{\text{peakL}}\text{-}C_{\min}, C_{\text{peakU}}\text{-}C_{\min})$ and $\lambda_m \sim U(0.7,1)$. Here, T_{peakL} (C_{peakL}) and T_{peakU} (C_{peakU}) are the lower and upper bounds of the peak values of temperature (H_2O concentration) for each inhomogeneity, respectively. $U(a,b)$ denotes uniform distribution in range (a,b).

As illustrated previously in Section III, the chord length matrix $\boldsymbol{L}$ is determined by the optical layout of the 32-beam TDLAS tomographic senor. Given the phantoms of 2-D temperature and H_2O concentration, path integrated absorbances $\boldsymbol{A}_{v_1} \in \mathbb{R}^{32\times1}$ and $\boldsymbol{A}_{v_2} \in \mathbb{R}^{32\times1}$ can be calculated according to the forward formulation described by (4). Finally, a sample, noted as $((\boldsymbol{A}_{v_1}, \boldsymbol{A}_{v_2}), \boldsymbol{T})$ is generated as a combination of the temperature vector $\boldsymbol{T} \in \mathbb{R}^{7592\times1}$ and corresponding path integrated absorbances $(\boldsymbol{A}_{v_1}, \boldsymbol{A}_{v_2})$ without noise contamination.

In this work, a dataset with a total of 10,900 samples is created, including 4,500 single-inhomogeneity phantoms (M=1) and 6,400 double-inhomogeneity phantoms (M=2). It is then randomly divided into a training set with 10,000 samples and a test set with 900 samples. Parameters in (16), (17) are set as $T_{\min}$=300 K, T_{peakL}=700 K, T_{peakU}=900 K, $C_{\min}$=0.01, C_{peakL}=0.11, and C_{peakU}=0.12. $\mu_{x,m} \sim U(34, 65)$, $\mu_{y,m} \sim U(34, 65)$ and $\sigma_m \sim U(10, 25)$ for $m \in \{1,...,M\}$. This operation is to increase the diversity of samples, and meanwhile, maintain the Gaussian inhomogeneities within the sensing region.

The network is trained using the noise-free training set. For the test set, to further characterize the real measurements, additional Gaussian noise is added to $\boldsymbol{A}_v$ as

$$\boldsymbol{A}_v += \delta \cdot \boldsymbol{n} \quad (18)$$

where $\boldsymbol{n} \in \mathbb{R}^{32\times1}$ is the noise vector conforming to standard distribution $G(0,1)$, and δ the standard deviation of the Gaussian noise converted from the specified Signal to Noise Ratio (SNR). Except for the noise-free test set, 6 additional test sets with different levels of noise are generated by ranging SNR from 20 dB to 45 dB with a step of 5 dB.

Simulated dataset with simple Gaussian profiles for both the temperature and H_2O mole fraction is used here to perform a proof-of-concept and lab-scale validation on the proposed network. If applied to reconstruct more complex temperature distributions in practice, the network needs to be re-trained accordingly with dataset established with computational fluid dynamics (CFD) aided data [32] or physically informed information [33].

B. Training of the Networks

Algorithm 2 summarizes the training process for the proposed QHT-LSTM. This is a combined training procedure for the coarse layer and fine layer of QHT-LSTM. Compared with separate training of a 1-LSTM-layer network for the coarse layer and a 3-LSTM-layer network for the fine layer, this procedure enables higher reconstruction accuracy for both the coarse-level reconstruction and the fine-level reconstruction.

In Algorithm 2, $\{((\boldsymbol{A}_{v_1,k}, \boldsymbol{A}_{v_2,k}), \boldsymbol{T}_k)$: k=1,2,...,$N_{\text{train}}\}$ represents the training set, where N_{train} is the number of training samples. E is the number of epochs, and α is the learning rate. The batch size B determines the number of batches N_{batch}, i.e. the number of iterations in one epoch for the mini-batch configuration, where $N_{\text{batch}} = \lfloor N_{\text{train}}/B \rfloor$. $\{((\boldsymbol{A}_{v_1,b}, \boldsymbol{A}_{v_2,b}), \boldsymbol{T}_b)$: b=1,2,...,$N_{\text{batch}}\}$ represents a batch, where $(\boldsymbol{A}_{v_1,b}, \boldsymbol{A}_{v_2,b}), \boldsymbol{T}_b)$ is a sample in it. $\bar{\boldsymbol{A}}_b$ is the sequence of vectors rearranged from $\boldsymbol{A}_{v_1,b}$ and $\boldsymbol{A}_{v_2,b}$ with Algorithm 1. $\boldsymbol{\Theta}^i_{\text{coarse}}$, $\boldsymbol{\Theta}^i_{\text{fine}}$, and $\boldsymbol{\Theta}^i$ denote the sets of trainable parameters updated by the i-th iteration, which are involved in the coarse layer $F_{\text{coarse}}(\cdot)$, the fine layer $F_{\text{fine}}(\cdot)$, and the entire QHT-LSTM, respectively. $\boldsymbol{\Theta}^i = \boldsymbol{\Theta}^i_{\text{coarse}} \cup \boldsymbol{\Theta}^i_{\text{fine}}$. $L(\boldsymbol{T}, \hat{\boldsymbol{T}})$ is defined to measure the Mean Square Error (MSE) loss of the reconstructed temperature vector $\hat{\boldsymbol{T}}$, corresponding to the true temperature vector $\boldsymbol{T}$, i.e.

Algorithm 2 The training process of QHT-LSTM

Input: training set $\{((\boldsymbol{A}_{v_1,k}, \boldsymbol{A}_{v_2,k}), \boldsymbol{T}_k)$: k=1,2,...,$N_{\text{train}}\}$, number of training samples N_{train}, number of epochs E, batch size B, and learning rate α.

Initialize: randomly initialize parameters in sets $\boldsymbol{\Theta}^0_{\text{coarse}}$ and $\boldsymbol{\Theta}^0_{\text{fine}}$,

$\boldsymbol{\Theta}^0 \leftarrow \boldsymbol{\Theta}^0_{\text{coarse}} \cup \boldsymbol{\Theta}^0_{\text{fine}}$

Number of batches $N_{\text{batch}} \leftarrow \text{floor}(N_{\text{train}}/B)$

Operations:

For l=1 to E **do**

Randomly split training set into batches of size B

For d=1 to N_{batch} **do**

Get the d-th batch $\{((\boldsymbol{A}_{v_1,b}, \boldsymbol{A}_{v_2,b}), \boldsymbol{T}_b)$: b=1,2,...,$B\}$

$i \leftarrow (l\text{-}1)\times N_{\text{batch}} + d$

For b=1 to B **do**

Rearrange $\boldsymbol{A}_{v_1,b}$ and $\boldsymbol{A}_{v_2,b}$ into the sequence of vectors $\bar{\boldsymbol{A}}_b$ with Algorithm 1;

Propagate forward $\bar{\boldsymbol{A}}_b$ through QHT-LSTM, output coarse-level reconstruction $\hat{\boldsymbol{T}}^b_{\text{coarse}}$ and fine-level reconstruction $\hat{\boldsymbol{T}}^b_{\text{fine}}$ as

$\hat{\boldsymbol{T}}^b_{\text{coarse}} \leftarrow F_{\text{coarse}}(\bar{\boldsymbol{A}}_b; \boldsymbol{\Theta}^{i\text{-}1}_{\text{coarse}})$

$\hat{\boldsymbol{T}}^b_{\text{fine}} \leftarrow F_{\text{fine}}(\bar{\boldsymbol{A}}_b; \boldsymbol{\Theta}^{i\text{-}1}_{\text{fine}})$

Calculate the coarse reconstruction loss $L^b_{\text{sample-coarse}}$ and fine reconstruction loss $L^b_{\text{sample-fine}}$ of the b-th sample as

$L^b_{\text{sample-coarse}} \leftarrow L(\boldsymbol{T}_b, \hat{\boldsymbol{T}}^b_{\text{coarse}})$

$L^b_{\text{sample-fine}} \leftarrow L(\boldsymbol{T}_b, \hat{\boldsymbol{T}}^b_{\text{fine}})$

End for

Calculate the coarse reconstruction loss $L^d_{\text{batch-coarse}}$ and fine reconstruction loss $L^d_{\text{batch-fine}}$ of the d-th batch as

$L^d_{\text{batch-coarse}} \leftarrow \frac{1}{B}\sum_{b=1}^{B} L^b_{\text{sample-coarse}}$

$L^d_{\text{batch-fine}} \leftarrow \frac{1}{B}\sum_{b=1}^{B} L^b_{\text{sample-fine}}$

Update the parameters in set $\boldsymbol{\Theta}^{i\text{-}1}_{\text{coarse}}$ by back propagation as

$\boldsymbol{\Theta}^{i}_{\text{coarse}} \leftarrow \text{Optimizer}(\boldsymbol{\Theta}^{i\text{-}1}_{\text{coarse}}; L^d_{\text{batch-coarse}}, \alpha)$

Update the parameters in set $\boldsymbol{\Theta}^{i}_{\text{fine}}$ by back propagation as

$\boldsymbol{\Theta}^{i}_{\text{fine}} \leftarrow \text{Optimizer}(\boldsymbol{\Theta}^{i\text{-}1}_{\text{fine}}; L^d_{\text{batch-fine}}, \alpha)$

$\boldsymbol{\Theta}^{i} \leftarrow \boldsymbol{\Theta}^{i}_{\text{coarse}} \cup \boldsymbol{\Theta}^{i}_{\text{fine}}$

End for

End for

Output: $\boldsymbol{\Theta}^i$

$$L(\boldsymbol{T}, \hat{\boldsymbol{T}}) = \frac{1}{|\boldsymbol{T}|}\left\|\hat{\boldsymbol{T}} - \boldsymbol{T}\right\|_2^2 \tag{19}$$

where $|\boldsymbol{T}|$ represents the length of temperature vector $\boldsymbol{T}$. $\|\cdot\|_2$ represents the L2 norm. $L^b_{\text{sample-coarse}}$ and $L^b_{\text{sample-fine}}$ denote the coarse and fine reconstruction losses of the b-th sample, respectively. $L^d_{\text{batch-coarse}}$ and $L^d_{\text{batch-fine}}$ denote the coarse and fine reconstruction losses of the d-th batch, respectively. Optimizer($\boldsymbol{\Theta}$; L, α) denotes the optimization algorithm used in the back propagation to update parameters in set $\boldsymbol{\Theta}$. Here, Adam optimizer [34] is employed.

According to the experimental results, the batch size B, learning rate α and the number of epochs E are empirically set as 32, 0.002, and 50, respectively. Leaky ReLU [35] is selected as the activation function $g(\cdot)$, defined as

$$g(x) = \max\{x, 0.01x\}. \tag{20}$$

The mean normalized reconstruction error over test set ξ_{test} is defined as

TABLE I

DEPENDENCE OF RELATIVE DECREASE OF ξ_{test} FOR THE COARSE-LEVEL OUTPUT AND FINE-LEVEL OUTPUT OF QHT-LSTM ON THE NUMBER OF LSTM LAYERS UNDER THE SNR OF 35 DB.

Number of LSTM layers	3	4	5
Relative decrease of ξ_{test} for the coarse-level output	3.64%	0.91%	0.93%
Relative decrease of ξ_{test} for the fine-level output	10.85%	0.87%	1.31%

TABLE II

HYPER-PARAMETERS OF THE H-CNN IMPLEMENTED IN THIS WORK.

	Input dim.	Output dim.	weight matrix size	Stride	Padding
Conv1	8×4×2	7×3×8	2×2	(1,1)	0
AP	7×3×8	6×2×8	2×2	(1,1)	0
Conv2	6×2×8	5×1×14	2×2	(1,1)	0
FC	70	7592	7592×70	-	-

$$\xi_{\text{test}} = \left(\frac{1}{N_{\text{test}}} \sum\nolimits_{k=1}^{N_{\text{test}}} \frac{\left\|\hat{\boldsymbol{T}}_k - \boldsymbol{T}_k\right\|_2}{\left\|\boldsymbol{T}_k\right\|_2} \right), \tag{21}$$

where N_{test} is the total number of samples in the test set. $\boldsymbol{T}_k$ and $\hat{\boldsymbol{T}}_k$ are the ground-true and reconstructed temperature vectors of the k-th sample in test set, respectively. Here, N_{test}=900.

When devising the architecture of QHT-LSTM, its specific settings are empirically chosen with simulations. Taking the SNR of 35 dB as example, Table I demonstrates the dependence of relative decrease of ξ_{test} for the coarse-level output and fine-level output of QHT-LSTM on the number of LSTM layers. The coarse-level reconstruction is fixed to be output from the first LSTM layer, while the fine-level reconstruction is output from the highest LSTM layer. In Table I, the values corresponding to l LSTM layers are the relative decrease of ξ_{test} when the number of LSTM layers is increased from l-1 to l. When the number of LSTM layer is increased from 2 to 3, the reconstruction accuracy, especially that of the fine-level output, is increased significantly. However, when the number of LSTM layers is larger than 3, its increment only brings slight gains in terms of the reconstruction accuracy. Simulations at other SNRs also shows similar results. Therefore, by trading off reconstruction accuracy with computational cost, the number of LSTM layers in QHT-LSTM is chosen as 3 in this work. Other settings, such as the number of FC layers and so on, are also chosen in this way.

To validate the performance of the proposed network, we compare QHT-LSTM with the CNN-based temperature reconstruction scheme proposed in [22], named as H-CNN here afterwards, which was a pioneer work of applying neural network in TDLAS tomography. Here, H-CNN is adapted for imaging temperature distribution in the octagonal sensing region from the LoS measurements obtained by the 32-beam sensor at the two transitions, as shown in Fig. 6. It consists of two convolutional layers, i.e. Conv1 and Conv2, one average pooling (AP) layer, and one fully-connected (FC) layer. Table II shows the empirically determined hyper-parameters of the H-CNN

implemented in this work. Other hyper-parameters such as the learning rate are set as the optimal values determined in [22].

Both H-CNN and the proposed QHT-LSTM are trained on the same training set with 10,000 noise-free samples constructed in Section IV. A. These two networks are implemented with Pytorch framework on a computer equipped with Intel i5-11300h CPU, 16G memory and NVIDA GeForce MX450.

C. Test Results

By feeding $(\boldsymbol{A}_{v_1}, \boldsymbol{A}_{v_2})$ of a test sample into the optimally trained H-CNN, $\widehat{\boldsymbol{T}}$ is output and reshaped into an image of the reconstructed temperature distribution. In contrast, by feeding $(\boldsymbol{A}_{v_1}, \boldsymbol{A}_{v_2})$ into the optimally trained QHT-LSTM, temperature vectors $\widehat{\boldsymbol{T}}_{\text{coarse}}$ and $\widehat{\boldsymbol{T}}_{\text{fine}}$ are output with different computational costs, respectively. Similarly, $\widehat{\boldsymbol{T}}_{\text{coarse}}$ and $\widehat{\boldsymbol{T}}_{\text{fine}}$ are reshaped into the coarse-quality and fine-quality images of temperature distributions in the sensing region, respectively.

Firstly, the temperature distributions reconstructed by QHT-LSTM and H-CNN are visually inspected. Fig. 7 and Fig. 8 demonstrate the reconstructed images of two representative phantoms, with a single Gaussian inhomogeneity in Fig. 7 (a) and two Gaussian inhomogeneities in Fig. 8 (a), at a practical SNR of 35 dB, respectively. Fig. 7 (b-d) and Fig. 8 (b-d) show images reconstructed using H-CNN, the coarse-quality and fine-quality images reconstructed using QHT-LSTM, respectively. For the single-inhomogeneity case, both H-CNN and QHT-LSTM can correctly locate the peak value in the sensing region. Compared with H-CNN, QHT-LSTM can more reliably indicate the profile of the inhomogeneity with fewer artefacts in both the coarse-quality and fine-quality images. For the double-inhomogeneity case, the temperature image reconstructed using H-CNN (Fig. 8 (b)) suffers from obvious distortion of the temperature profile. In contrast, the two images reconstructed by QHT-LSTM can correctly indicate the temperature profile. The fine-quality temperature image (Fig. 8 (d)) shows much stronger consistency with the phantom in both the amplitudes of the higher and lower temperature peaks.

Then, the performances of QHT-LSTM and H-CNN are quantitatively evaluated at different SNRs.

Fig. 9 shows the dependence of ξ_{test} on SNRs obtained from H-CNN, the coarse-level and the fine-level outputs of QHT-LSTM, respectively. As shown in Fig. 9, ξ_{test} decreases as SNR increases for both H-CNN and QHT-LSTM. At all levels of noise, ξ_{test} of both the coarse-level and the fine-level outputs of QHT-LSTM are always smaller than that obtained by H-CNN, indicating both the coarse-quality and the fine-quality temperature distributions reconstructed by QHT-LSTM have better fidelity than that reconstructed by H-CNN. ξ_{test} of the fine-level output of QHT-LSTM is always the smallest among all the three. Taking the SNR of 35 dB as an example, ξ_{test} obtained by H-CNN, the coarse-level and the fine-level outputs of QHT-LSTM are 0.0564, 0.0318 and 0.0238, respectively. In comparison with H-CNN, the coarse-level and the fine-level outputs of QHT-LSTM suppress the

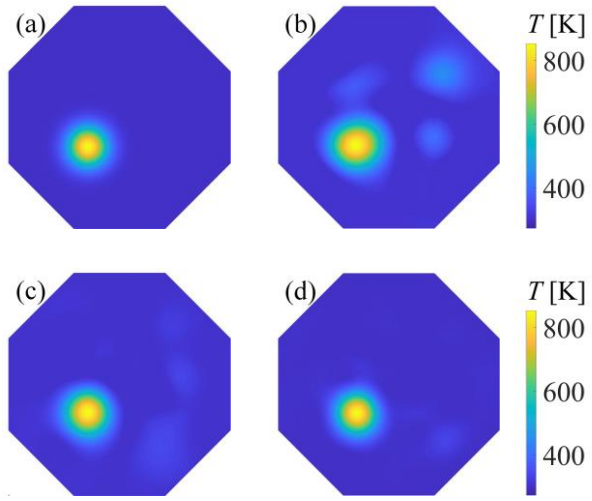

Fig. 7. Reconstruction of temperature images for a single-inhomogeneity phantom at an SNR of 35 dB. (a) shows the true temperature image. (b-d) show images reconstructed using H-CNN, the coarse-quality and fine-quality images reconstructed using QHT-LSTM, respectively.

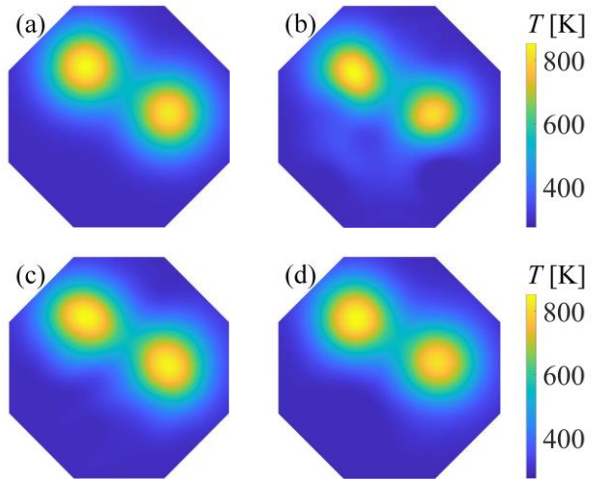

Fig. 8. Reconstruction of temperature images for a double-inhomogeneity phantom at an SNR of 35 dB. (a) shows the true temperature image. (b-d) show images reconstructed using H-CNN, the coarse-quality and fine-quality images reconstructed using QHT-LSTM, respectively.

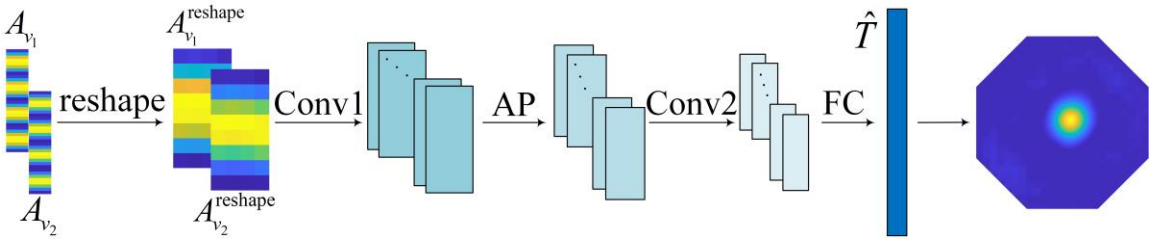

Fig. 6 Architecture of the H-CNN adapted to the reconstruction situation discussed in this work.

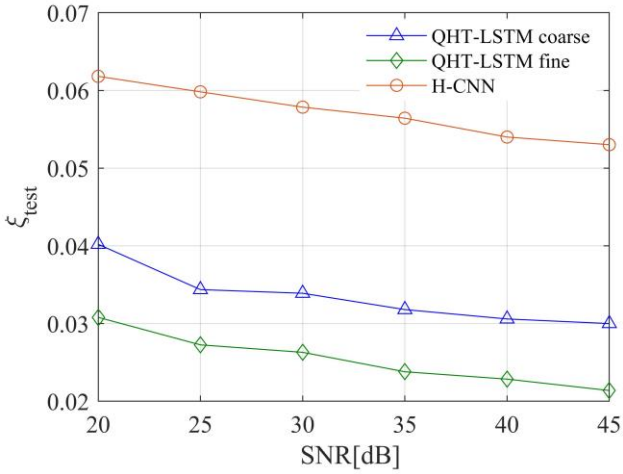

Fig. 9. Dependence of ξ_{test} on SNRs for H-CNN, coarse-level output and fine-level output of QHT-LSTM.

TABLE III
COMPARISON OF THE TIME ELAPSED FOR TRAINING AND SINGLE-FRAME IMAGE RECONSTRUCTION USING H-CNN AND QHT-LSTM.

Network	QHT-LSTM coarse level	QHT-LSTM fine level	H-CNN
Training time (min)	8.3		1.5
Average time elapsed for single-frame image reconstruction (sec)	0.036×10^{-3}	0.111×10^{-3}	0.017×10^{-3}

reconstruction error by 43.62% and 57.80%, respectively.

Finally, the time elapsed for training and a single-frame image reconstruction using H-CNN and QHT-LSTM are compared in Table III. The training and a single-frame image reconstruction time of QHT-LSTM are longer than those of H-CNN. It is caused by the deeper structure of QHT-LSTM, established to achieve lower reconstruction error, in comparison with H-CNN. It is worth mentioning the time elapsed for image reconstruction, that determines the temporal response of the TDLAS tomographic system, is critical in practical application. As shown in Table III, a single-frame image reconstruction from the coarse-level output of QHT-LSTM takes 0.036 millisecond (ms), denoting a real-time temporal resolution of more than 27k frames per second (kfps) can be achieved. This capability is very beneficial for time resolved measurements of turbulence-chemistry interactions occurring at the medium-to-large scales [36]. On the other hand, although the single-frame image reconstruction from the fine-level output of QHT-LSTM triples the coarse-level scenario, the better image quality achieved by the fine-level output provides much accurate features of the flame, enabling offline analysis of the reactive process for combustion optimization.

V. EXPERIMENT

Lab-scale experiments were carried out to further validate the performance of the proposed QHT-LSTM. The 32-beam TDLAS tomographic sensor was built with the optical layout shown in Fig. 2. More details of the optics and hardware

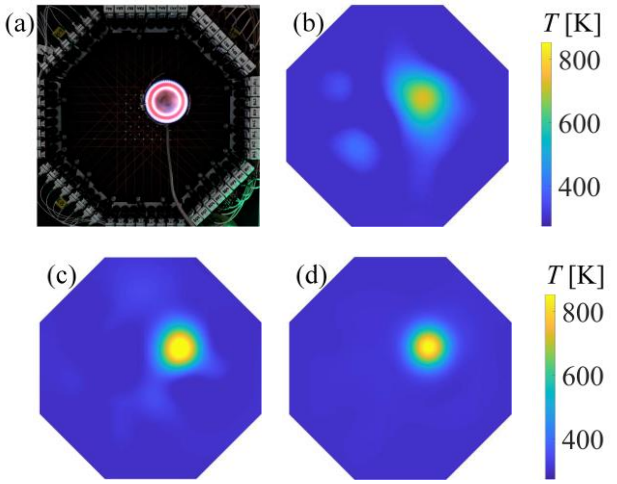

Fig. 10. Reactive flow field generated in the experiment with (a) a single inhomogeneity, (b) the temperature image reconstructed using H-CNN, (c) and (d) the coarse-quality and fine-quality temperature images reconstructed using QHT-LSTM.

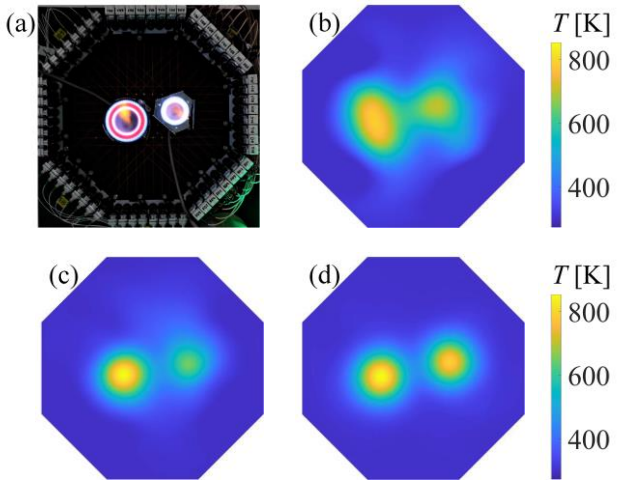

Fig. 11. Reactive flow field generated in the experiment with (a) two inhomogeneities, (b) the temperature image reconstructed using H-CNN, (c) and (d) the coarse-quality and fine-quality temperature images reconstructed using QHT-LSTM.

electronics have been described in our previous publications [8, 29]. Similar as the simulation, two representative cases with single-inhomogeneity and double-inhomogeneity temperature distributions are demonstrated in the experiment. Fig. 10 (a) shows the single-inhomogeneity case with a flame located at the right-upper centre of the sensing region, while Fig. 11 (a) shows the double-inhomogeneity case with a larger-size flame located left and a smaller-size flame upper right in the sensing region.

For the single-inhomogeneity case, the temperature image reconstructed by H-CNN is shown in Fig. 10 (b). The coarse-quality and fine-quality temperature images reconstructed by the proposed QHT-LSTM are shown in Figs. 10 (c) and (d), respectively. For each of the three reconstructed images, the retrieved peak position agrees well with that of the real flame. The amplitudes of the peak temperature are also consistent in the three images, giving 686 K, 895 K and 819 K in Figs. 10 (b), (c) and (d), respectively. However, the two images retrieved using

the proposed QHT-LSTM have fewer artefacts in comparison with that retrieved using H-CNN. Furthermore, the fine-quality reconstruction image (Fig. 10 (d)) gives the clearest temperature profile and the heat dissipation from the hot zone.

For the double-inhomogeneity case, both H-CNN and QHT-LSTM can correctly locate the peak position of the larger-size flame. The amplitudes of the peak temperature of the larger-size flame are also consistent in the three images, giving 742 K, 841 K and 779 K in Figs. 11 (b), (c) and (d), respectively. As the larger-size flame is the same as that used in Fig. 10, the retrieved values of peak temperature using the QHT-LSTM, especially that in the fine-quality reconstruction, show better agreement with the single-inhomogeneity case. However, H-CNN fails for retrieval of the smaller-size flame since the reconstructed object suffers from strong interference by its neighboring artifacts. In contrast, both the coarse-quality image and the fine-quality image reconstructed using QHT-LSTM can correctly locate the position of the small-size flame.

In fact, computational tomographic algorithms and data-driven tomographic algorithms are designed under different prerequisites. Data-driven tomographic algorithms are developed for applications where *a priori* information of the target flows can be assumed or known. Consequently, the *a priori* information can facilitate the establishment of appropriate dataset to train the network, thus leading to accurate reconstructions. In contrast, computational tomographic algorithms are good at performing reconstruction even with inadequate *a priori* information, but generally suffer from rank deficiency in TDLAS tomography due to the limited number of available projection data. As a result, poorer reconstruction accuracy is generally obtained by computational tomographic algorithms. Therefore, these two categories of tomographic algorithms are scenario-dependent and cannot be directly compared in terms of reconstruction accuracy.

VI. Conclusion

A novel quality-hierarchical temperature image network based on stacked LSTM, named as QHT-LSTM, is proposed for TDLAS tomography. To facilitate the progressive inverse mapping, the input of QHT-LSTM is sequential vectors rearranged from LoS TDLAS measurements, considering the spatial similarity inherently incurred by the optical layout of TDLAS tomographic sensor. QHT-LSTM reconstructs two temperature images, i.e. a coarse-quality image and a fine-quality image, to describe the temperature profiles by trading off the accuracy and computational cost.

The performance of QHT-LSTM is evaluated using the simulated test sets and the lab-scale experiments, and compared with the recently published model H-CNN. Simulated and experimental results show that both the coarse-level and the fine-level outputs of QHT-LSTM outperform H-CNN in image fidelity. With the capability of tens of kfps-level imaging, the coarse-level output is substantially indicative for real-time combustion monitoring and active control. Furthermore, the fine-quality images reconstructed by QHT-LSTM is stronger at revealing spatial details than the coarse-quality images, at a cost of tripling the reconstruction time.

References

[1] M. P. Wood and K. B. Ozanyan, "Simultaneous temperature, concentration, and pressure imaging of water vapor in a turbine engine," *IEEE Sens. J.*, vol. 15, no. 1, pp. 545-551, 2015.

[2] N. Terzija, S. Karagiannopoulos, S. Begg, P. Wright, K. Ozanyan, and H. McCann, "Tomographic imaging of the liquid and vapour fuel distributions in a single-cylinder direct-injection gasoline engine," *Int. J. Engine Res.*, vol. 16, no. 4, pp. 565-579, 2015.

[3] C. Liu, Z. Cao, Y. Lin, L. Xu, and H. McCann, "Online cross-sectional monitoring of a swirling flame using TDLAS tomography," *IEEE T. Instrum. Meas.*, vol. 67, no. 6, pp. 1338-1348, 2018.

[4] Q. Qu, Z. Cao, L. Xu, C. Liu, L. Chang, and H. McCann, "Reconstruction of two-dimensional velocity distribution in scramjet by laser absorption spectroscopy tomography," *Appl. Opt.*, vol. 58, no. 1, pp. 205-212, 2019.

[5] H. Xia *et al.*, "Two-step tomographic reconstructions of temperature and species concentration in a flame based on laser absorption measurements with a rotation platform," *Optics and Lasers in Engineering*, vol. 90, pp. 10-18, 2017.

[6] T. Yu, and W. Cai, "Benchmark evaluation of inversion algorithms for tomographic absorption spectroscopy," *Applied Optics*, vol. 56, no. 8, pp. 2183-2194, 2017.

[7] W. Q. Yang, D. M. Spink, T. A. York, and H. McCann, "An image-reconstruction algorithm based on Landweber's iteration method for electrical-capacitance tomography," *Measurement Science and Technology*, vol. 10, no. 11, pp. 1065-1069, 1999.

[8] Y. Bao *et al.*, "Relative Entropy Regularized TDLAS Tomography for Robust Temperature Imaging," *IEEE Transactions on Instrumentation and Measurement*, vol. 70, pp. 1-9, 2021.

[9] C. Liu, and L. Xu, "Laser absorption spectroscopy for combustion diagnosis in reactive flows: A review," *Applied Spectroscopy Reviews*, vol. 54, no. 1, pp. 1-44, 2019.

[10] K. Wang, F. Li, H. Zeng, and X. Yu, "Three-dimensional flame measurements with large field angle," *Opt Express*, vol. 25, no. 18, pp. 21008-21018, Sep 4 2017.

[11] W. Cai and C. F. Kaminski, "A numerical investigation of high-resolution multispectral absorption tomography for flow thermometry," *Applied Physics B*, vol. 119, no. 1, pp. 29-35, 2015.

[12] J. Dai, S. O'Hagan, H. Liu, W. Cai, and P. Ewart, "Hyperspectral tomography based on multi-mode absorption spectroscopy (MUMAS)," *Applied Physics Letters*, vol. 111, no. 18, pp. 184102-1-184102-5, 2017.

[13] Y. LeCun, Y. Bengio, and G. Hinton, "Deep learning," *Nature*, vol. 521, no. 7553, pp. 436-44, May 28 2015.

[14] J. Schmidhuber, "Deep learning in neural networks: an overview," *Neural Netw*, vol. 61, pp. 85-117, Jan 2015.

[15] A. V. Sozykin, "An Overview of Methods for Deep Learning in Neural Networks," *Bulletin of the South Ural State University. Series "Computational Mathematics and Software Engineering"*, vol. 6, no. 3, pp. 28-59, 2017.

[16] T. Qiu, M. Liu, G. Zhou, L. Wang, and K. Gao, "An Unsupervised Classification Method for Flame Image of Pulverized Coal Combustion Based on Convolutional Auto-Encoder and Hidden Markov Model," *Energies*, vol. 12, no. 13, 2019.

[17] Y. Jin *et al.*, "Three-dimensional rapid flame chemiluminescence tomography via deep learning," *Opt Express*, vol. 27, no. 19, pp. 27308-27334, Sep 16 2019.

[18] J. Huang, H. Liu, and W. Cai, "Online in situ prediction of 3-D flame evolution from its history 2-D projections via deep learning," *Journal of Fluid Mechanics*, vol. 875, 2019.

[19] C. Wei, K. K. Schwarm, D. I. Pineda, and R. M. Spearrin, "Deep neural network inversion for 3D laser absorption imaging of methane in reacting flows," *Opt Lett*, vol. 45, no. 8, pp. 2447-2450, Apr 15 2020.

[20] T. Yu, H. Liu, J. Zhang, W. Cai, and F. Qi, "Toward real-time volumetric tomography for combustion diagnostics via dimension reduction," *Opt Lett*, vol. 43, no. 5, pp. 1107-1110, Mar 1 2018.

[21] T. Yu, W. Cai, and Y. Liu, "Rapid tomographic reconstruction based on machine learning for time-resolved combustion diagnostics," *Rev Sci Instrum*, vol. 89, no. 4, p. 043101, Apr 2018.

[22] J. Huang, H. Liu, J. Dai, and W. Cai, "Reconstruction for limited-

data nonlinear tomographic absorption spectroscopy via deep learning," *Journal of Quantitative Spectroscopy and Radiative Transfer*, vol. 218, pp. 187-193, 2018.

[23] J. Huang, J. Zhao, and W. Cai, "Compressing convolutional neural networks using POD for the reconstruction of nonlinear tomographic absorption spectroscopy," *Computer Physics Communications*, vol. 241, pp. 33-39, 2019.

[24] Y. Jiang *et al.*, "CSTNet: a dual-branch convolutional network for imaging of reactive flows using chemical species tomography," *Submitted to IEEE Transactions on Neural Networks and Learning Systems*, arXiv:2010.03868

[25] J. Si *et al.*, "Hierarchical Temperature Imaging Using Pseudo-Inversed Convolutional Neural Network Aided TDLAS Tomography", *IEEE Transactions on Instrumentation and Measurement*, DOI: 10.1109/TIM.2021.3110282.

[26] S. Hochreiter and J. Schmidhuber, "Long short-term memory," *Neural Comput*, vol. 9, no. 8, pp. 1735-80, Nov 15 1997.

[27] S. Zhang *et al*, "On Geometric Features for Skeleton-Based Action Recognition Using Multilayer LSTM Networks," *in Applications of Computer Vision*, 2017.

[28] J. Si *et al.*, "A quality-hierarchical temperature imaging network for TDLAS tomography" presented at *IEEE International Instrumentation and Measurement Technology Conference (I2MTC)*, Glasgow, United Kingdom, May 17-20, 2021.

[29] G. Enemali, R. Zhang, H. Mccann, and C. Liu, "Cost-Effective Quasi-Parallel Sensing Instrumentation for Industrial Chemical Species Tomography," *IEEE Transactions on Industrial Electronics*, 2021.

[30] C. Liu, L. Xu, Z. Cao, and H. McCann, "Reconstruction of axisymmetric temperature and gas concentration distributions by combining fan-beam TDLAS with onion-peeling deconvolution," *IEEE T. Instrum. Meas.*, vol. 63, no. 12, pp. 3067-3075, 2014.

[31] C. Liu, L. Xu, J. Chen, Z. Cao, Y. Lin, and W. Cai, "Development of a fan-beam TDLAS-based tomographic sensor for rapid imaging of temperature and gas concentration," *Opt. Express*, vol. 23, no. 17, pp. 22494-22511, 2015.

[32] C. Wei, K. K. Schwarm, D. I. Pineda, and R. Mitchell Spearrin, "Physics-trained neural network for sparse-view volumetric laser absorption imaging of species and temperature in reacting flows," Opt Express, vol. 29, no. 14, pp. 22553-22566, Jul 5 2021.

[33] J. P. Molnar and S. J. Grauer, "Flow Field Tomography with Uncertainty Quantification using a Bayesian Physics-Informed Neural Network," arXiv preprint, arXiv:2108.09247, 2021.

[34] D. P. Kingma and J. Ba, "Adam: A Method for Stochastic Optimization," *Proceedings of the 3rd International Conference on Learning Representations (ICLR)*, 2014.

[35] K. He, X. Zhang, S. Ren, and J. Sun, "Delving Deep into Rectifiers: Surpassing Human-Level Performance on ImageNet Classification," *Proceedings of the IEEE International Conference on Computer Vision (ICCV)*, pp. 1026-1034, 2015.

[36] I. Boxx, C. D. Carter, M. Stöhr, and W. Meier, "Study of the mechanisms for flame stabilization in gas turbine model combustors using kHz laser diagnostics," *Experiments in Fluids*, vol. 54, no. 5, pp. 1-17, 2013.

Jingjing Si (Member, IEEE) received the B.S. degree in electronic engineering and the M.S. degree in communication and information system from Yanshan University, Hebei, China, in 2002 and 2005, respectively, and the Ph.D. degree in communication and information system from Beijing University of Posts and Telecommunications, Beijing, China, in 2010. Since 2002, she has been with the School of Information Science and Engineering, Yanshan University, where she is currently a Professor. Her current research interests include multimedia signal processing, inverse problem, and optimization.

Gengchen Fu received the B.S. degree in electronic and information engineering from North China University of Science and Technology, Hebei, China, in 2019. Currently, he is pursuing the M.S. degree with the School of Information Science and Engineering, Yanshan University, Hebei, China. His research interest is focused on laser absorption spectroscopic tomography.

Yinbo Cheng received the B.S. and M.S. degrees in computer software and theory from Yanshan University, Hebei, China, in 1999 and 2005, respectively, and the Ph.D. degree in communication and information system from Beijing University of Posts and Telecommunications, Beijing, China, in 2010. From 2013 to 2017, he was a Post-Doctoral Researcher with Yanshan University. Since 2017, he has been a Lecturer with the Ocean Collage, Hebei Agricultural University, Hebei, China. His current research interests include big data analytic, data mining, and machine learning.

Rui Zhang received the B.Eng. degree (Hons.) in electronics and electrical engineering with management from The University of Edinburgh, Edinburgh, U.K., in 2019, and the B.Eng. (Hons.) degree in Internet of Things engineering from Tianjin University, Tianjin, China, in 2019. She is currently pursuing the Ph.D. degree with the Agile Tomography Group, School of Engineering, The University of Edinburgh. Her current research interest is focused on laser absorption spectroscopic tomography with a customized spatial resolution for combustion diagnose.

Godwin Enemali (Member, IEEE) received the B.Eng. degree (Hons.) in electrical and electronics engineering from the University of Agriculture Makurdi, Makurdi, Nigeria, in 2010, and the M.Sc. and Ph.D. degrees in electronics engineering from The University of Edinburgh, Edinburgh, U.K., in 2014 and 2019, respectively. Since 2018, he has been a Research Associate with the Agile Tomography Group, Institute for Digital Communication, The University of Edinburgh. His current research focuses on high-speed data acquisition systems, reliable FPGA-based system implementation, laser absorption spectroscopy (LAS), and chemical species tomography.

Chang Liu (Member, IEEE) received the B.Sc. degree in automation from Tianjin University, Tianjin, China, in 2010, and the Ph.D. degree in testing, measurement technology and instrument from Beihang University, Beijing, China, in 2016. From April 2016 to January 2018, he was a Post-Doctoral Researcher with the Department of Air Pollution and Environmental Technology, Empa-Swiss Federal Laboratories for Materials Science and Technology, Dübendorf, Switzerland. Since February 2018, he has been a Lecturer with the School of Engineering, The University of Edinburgh, Edinburgh, U.K. His current research interests include NIR/MIR laser absorption spectroscopy (LAS), active/passive optical tomography techniques and system design, and their applications to combustion diagnosis and environmental monitoring.